



Title	Seismic and infrasound monitoring of Bowdoin Glacier, Greenland
Author(s)	Podolskiy, Evgeny A.; Genco, Riccardo; Sugiyama, Shin; Walter, Fabian; Funk, Martin; Minowa, Masahiro; Tsutaki, Shun; Ripepe, Maurizio
Citation	低温科学, 75, 15-36
Issue Date	2017-03-31
DOI	10.14943/lowtemsci.75.15
Doc URL	http://hdl.handle.net/2115/65007
Type	bulletin (article)
File Information	4_15-36.pdf



[Instructions for use](#)

Seismic and infrasound monitoring of Bowdoin Glacier, Greenland

**Evgeny A. Podolskiy^{1*}, Riccardo Genco², Shin Sugiyama³, Fabian Walter⁴,
Martin Funk⁴, Masahiro Minowa³, Shun Tsutaki^{5,6}, Maurizio Ripepe²**

Received 28 October 2016, accepted 11 January 2017

Outlet glaciers in Greenland have retreated and lost mass over the past decade. Understanding the dynamics of tidewater glaciers is crucial for forecasting sea-level rise and for understanding the future of the Greenland Ice Sheet, given the buttressing support that tidewater glaciers provide to inland ice. However, the mechanisms controlling glacier-front location and the role played by external forcings (e.g., meltwater input and tidal oscillation) in basal motion and fracture formation leading to iceberg calving are poorly understood. Today it is known that glaciers generate seismic and infrasound signals that are detectable at local and teleseismic distances and can be used to monitor glacier dynamics. Here, we present examples of data recorded by a temporary network of seismic and infrasound instruments deployed at a tidewater glacier (Bowdoin Glacier, Greenland) in July 2015. Some stations were installed on ice at distances as close as ~ 250 m from the calving front, representing the closest deployments to the calving front that have been made to date. Multiple seismic and infrasound events were recorded by five seismic and six infrasound sensors, and linked to surface crevassing, calving, and ice-cliff collapses, and presumably also hydrofracturing, iceberg rotations, teleseismic earthquakes, and helicopter-induced tremors. Using classic seismological and array analysis approaches (e.g., “short-term averaging/long-term averaging” and “ $f-k$ ” analysis), as well as image processing techniques, we explore this unique dataset to understand the glacial response to external forcings. Our observations, supported by GPS measurements of ice velocity, local weather-station records, and time-lapse photography, provide a valuable resource for studying seismogenic glacial processes and their dependence on ocean tides and other environmental factors.

Keywords: Seismicity, infrasound, array, tidewater glacier, Greenland

1. Introduction

“Beneath our feet a continuous trembling sensation was felt ... Quick, sharp, deep-tingling, ringing, shrieking

sounds frightful enough, came, not as sound usually does, horizontally, but vertically up to our ears, seeming to vibrate through our feet, our limbs, our very bodies, spitefully shouting in our ears: Why, presump-

*Corresponding author

e-mail : e.podolskiy@arc.hokudai.ac.jp

1) Arctic Research Center, Hokkaido University, Sapporo, Japan

2) Dipartimento di Scienze della Terra, Università di Firenze, Florence, Italy

3) Institute of Low Temperature Science, Hokkaido University, Sapporo, Japan

4) Laboratory of Hydraulics, Hydrology and Glaciology, ETH Zürich, Zurich, Switzerland

5) Earth Observation Research Center, Japan Aerospace Exploration Agency, Tsukuba, Japan

6) Arctic Environment Research Center, National Institute of Polar Research, Tachikawa, Japan

tuous man, hast thou set disturbing foot upon my chaste bosom? Beware! Beware! Beware! Split-jingle-crash-Off! Away! Away!"

E. B. Baldwin about his crossing of the Bowdoin Glacier in the summer 1894 (Baldwin, 1896)

Polar glaciers are difficult and expensive to access for scientific research purposes. Moreover, glacier interiors are difficult environments in which to study and monitor important glacial phenomena such as the dynamics of ice fracturing, the mechanisms of basal movement, and the material properties of ice and sub-glacial till, as well as the evolution of sub-glacial drainage systems. Similarly, the observation of calving-rates remains challenging and is one of the most uncertain inputs in predictions of future sea-level rise (IPCC, 2013).

In this light, passive seismology enables monitoring of near- and sub-surface processes at high spatial and temporal resolutions in regions that are difficult to access or hard to monitor. Recent observational studies have shown that monitoring the natural seismicity of ice is useful for many glaciological applications (for a comprehensive review, see Podolskiy and Walter, 2016). In particular, seismological techniques have been applied to the study of the Greenland Ice Sheet (GrIS) and its marginal ice and glaciers, which are known to have experienced retreat and intense mass loss in the last decade (Khan et al., 2015). For example, if we limit ourselves only to Greenland-related research, Ekström et al. (2003) reported previously unknown tele-seismic events that differ from tectonic earthquakes, termed “glacier earthquakes”, which are generated by large-scale iceberg calving and capsizing events. These events have increased in frequency since 1990 (Ekström et al., 2006), and their locations have spread into northwest Greenland during the last decade (Veitch and Nettles, 2012). In another context, Walter et al. (2014) showed that the properties and thickness of sub-glacial sediments, which influence basal movement, could be estimated beneath the margin of western Greenland via analysis of natural seismicity. Bartholomäus et al. (2015) demonstrated the possibility of quantifying sub-glacial discharge using continuous seismic tremor as a proxy. Carmichael et al. (2015) analyzed seismic and

GPS signals related to the rapid draining of a supra-glacial lake, and associated the signals with an increase in ice-flow speed in western Greenland. Their results suggested that the ice-quake activity peak was associated with vertical hydro-fracturing that enhanced ice flow by supplying meltwater from the lake to the bed at a depth of almost 1 km. Roeoesli et al. (2016) discovered small stick-slip events that are influenced by meltwater input, which were previously never observed near the base of the Greenland Ice Sheet. Furthermore, most recently, Mordret et al. (2016) demonstrated that the mass balance of Southern Greenland could be inferred from ambient seismic-noise analysis. This innovative approach is based on measurements of seismic-velocity variations in the crust due to changes in ice-mass loading. According to the authors, this technique presents an opportunity for near-real-time mass-balance monitoring as an alternative to satellite observations, which have limited temporal resolution.

Glacial seismic sources corresponding to sudden mass acceleration also emit energy into the atmosphere in the form of infrasound waves; i.e., as air-pressure oscillations at frequencies below 20 Hz, which can propagate for thousands of kilometers with little attenuation. In particular, calving and iceberg capsizing events are the most prominent sources of local and regional infrasound and seismic wave fields at regional and tele-seismic scales (e.g., Richardson et al., 2010). Analysis of both types of signals allows for a comprehensive understanding of the source mechanisms and source location in time and space. Specifically, the different information carried by seismic waves propagating through solid ice and infrasound waves propagating through air from the same event, which may involve impacts and mass acceleration, has the potential to provide additional insights. Moreover, infrasound data can be a useful complement to seismic data as it helps to better differentiate surface events like iceberg calving from signals emanating from other parts of the glacier. To our knowledge, the possibility of glacial and cryosphere monitoring with infrasound remains to be explored, and has only rarely been applied previously (Richardson et al., 2010; Maruyama et al., 2015; Preiswerk et al., 2016).

The internationally funded Greenland Ice Sheet

Monitoring Network (GLISN) currently provides continuous regional seismic observations in Greenland, including near-real-time data from some of its stations. These data are freely distributed by Incorporated Research Institutions for Seismology (IRIS). However, local observations are needed to obtain a comprehensive understanding of glacier dynamics and glacier seismic sources, especially because the magnitude of most events is too weak (i.e., $M < 1$) to be detected at epicentral distances greater than a few kilometers (Podolskiy and Walter, 2016). Moreover, a long-term Comprehensive Nuclear-Test-Ban Treaty Organization (CTBTO) infrasound installation (IS18) for real-time nuclear and atmospheric monitoring, located near Qaanaaq village in northwestern Greenland, provides detailed in-situ infrasound observations that are valuable for assessing the potential, and limitations, of using this geophysical approach for cryospheric studies.

Against this background, in this paper we briefly introduce the seismic and infrasound monitoring campaign that we conducted at Bowdoin Glacier in northwestern Greenland in July 2015. This work formed part of a comprehensive set of glaciological observations, organized as a collaboration among Hokkaido University (Japan), ETH Zürich (Switzerland), and the University of Florence (Italy). A similar field campaign was performed in July 2016, and the results will be published elsewhere, along with a detailed analysis of the present results.

2. Site and instrumentation set-up

2.1 Study site

Bowdoin Glacier ($77^{\circ}41'N$, $68^{\circ}35'W$) is located ~ 125 km from Pituffic and more than 25 km from Qaanaaq. The glacier was named after Bowdoin College, USA, by its famous 1877 graduate, Arctic explorer Admiral Robert Peary. It is a grounded tide-water glacier with a calving front that is 3 km wide. The first scientific observations of the glacier were performed during Peary's expedition of 1894, and included, surprisingly, time-lapse photography. These observations are described in the corresponding expedition reports (Chamberlin, 1895; Chamberlin, 1897). The latter report presented photographs of the glacier front, near-

front ice-speed measurements of up to 84 cm per day at the center and 57 cm per day on average, and other detailed, mostly qualitative descriptions. Since 2013, the dynamics of Bowdoin Glacier and the properties of its fjord have been intensively studied through annual Japanese expeditions and from satellite imagery (Sugiyama et al., 2015). These more recent observations have found that the terminus of the glacier remained relatively stable until 2008, when it started to retreat from an elongate submarine bump oriented perpendicular to the fjord. Close to the calving front, ice thickness measured with ground-penetrating radar is known to be less than 280 m. Precise GPS measurements show that the horizontal ice speed is tide-modulated and reaches a maximum of ~ 2 m per day at low tide (Sugiyama et al., 2015).

2.2 Instrumentation

Despite some heavily crevassed zones, conditions in the lower parts of the glacier surface enable many locations to be accessed by foot, thus permitting direct access to the calving front and creating various unique opportunities for deploying monitoring instruments. In July 2015, several sites (both on the ice and on nearby rock outcrops along the eastern side of the glacier) were selected for observations, to enable near-source monitoring of calving front dynamics (Fig. 1). A helicopter was used to transport instrumentation to monitoring sites and to deliver seismic-array equipment to a location on the central moraine a few hundred meters from the calving front (Fig. 2). The ability to land a helicopter near the calving front on the loose boulders of the moraine and the availability of human resources to manually move heavy equipment over the rough ice surface with backpacks were crucial to the successful and safe installation of the on-ice seismic array. This seismic deployment is closer to the calving front than any previous set-up.

A Guralp CMG40T triaxial broadband seismometer, sensitive to periods up to 30 s, was installed on the rocky coast forward of the calving front, along with a Guralp CMG-DAS-S6 recorder operating at a sampling rate of 100 Hz and a GoPro time-lapse camera operating at 6 frames per minute. An Onset HOBO U-20 water-pressure sensor, operating at a sampling rate of 0.5 Hz,

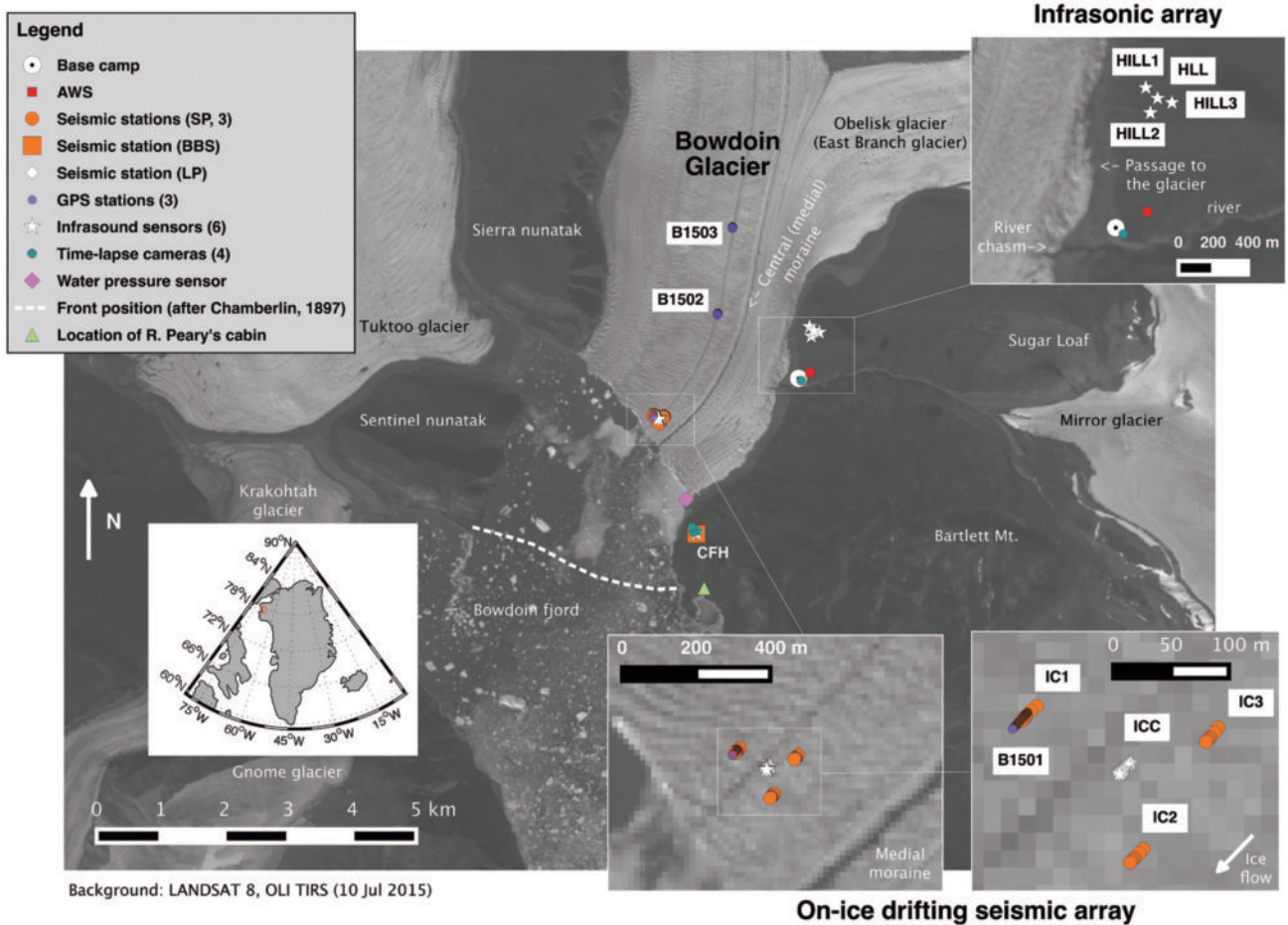


Figure 1 : Map of the Bowdoin Glacier geophysical experiment setup of July 7–19, 2015. The insets at lower right show close-up views of the seismic array. Note that a drift in the position of the on-ice stations is apparent due to the ice flow. Depending on the station, these shifts corresponds to $\sim 14\text{--}18$ m of horizontal displacement in total. The inset at lower left shows a map of Greenland with Bowdoin’s location.

was deployed in the fjord to record micro-tsunamis generated by calving events. Four Lennartz LE-3D short-period (SP) and long-period (LP) seismometers, connected to Taurus/Nanometrics and Guralp data loggers, were arranged on the glacier ice in a triangular array located ~ 250 m from the marginal ice cliff, where icebergs are discharged into the fjord. The three SP stations (named “IC1”, “IC2”, and “IC3”) used seismometers with a natural frequency of 1 Hz, and formed the vertices of the triangular array. The instruments were seated on tripods, as used typically for installations into soft soil. The central LP station (“ICC”) used an instrument with a natural frequency of 0.2 Hz that was placed on a ceramic tile. All stations operated at a sampling rate of 500 Hz. Each sensor was placed in an ice pit with a drainage channel for removing meltwater; each pit was covered with a metal mesh and a high-albedo blanket to protect the stations from wind, rain,

and solar radiation (Fig. 2).

An infrasound array, comprising four absolute pressure transducers (from iTem geophysics) with a sensitivity of 0.01 Pa in the 0.01–100 Hz frequency band, was installed on a hill located close to the base camp, 3 km behind the calving front and at an elevation of 270 m. Three pressure sensors were connected via 100 m cables to a Guralp data-logger (7 channels, 24 bits Guralp CMG-DM24 A/D converter), operating at a sampling frequency of 500 Hz, located at the central station. Another two infrasound sensors were co-located with the central station of the on-ice seismic array, ICC, and the broadband seismic station, recording at sampling rates of 500 and 100 Hz, respectively. The aperture of both arrays was ~ 150 m. In addition, three dual-frequency GPS stations (Global Navigation Satellite Systems, GEM-1) were deployed on the ice, and a reference station was positioned on bedrock to establish

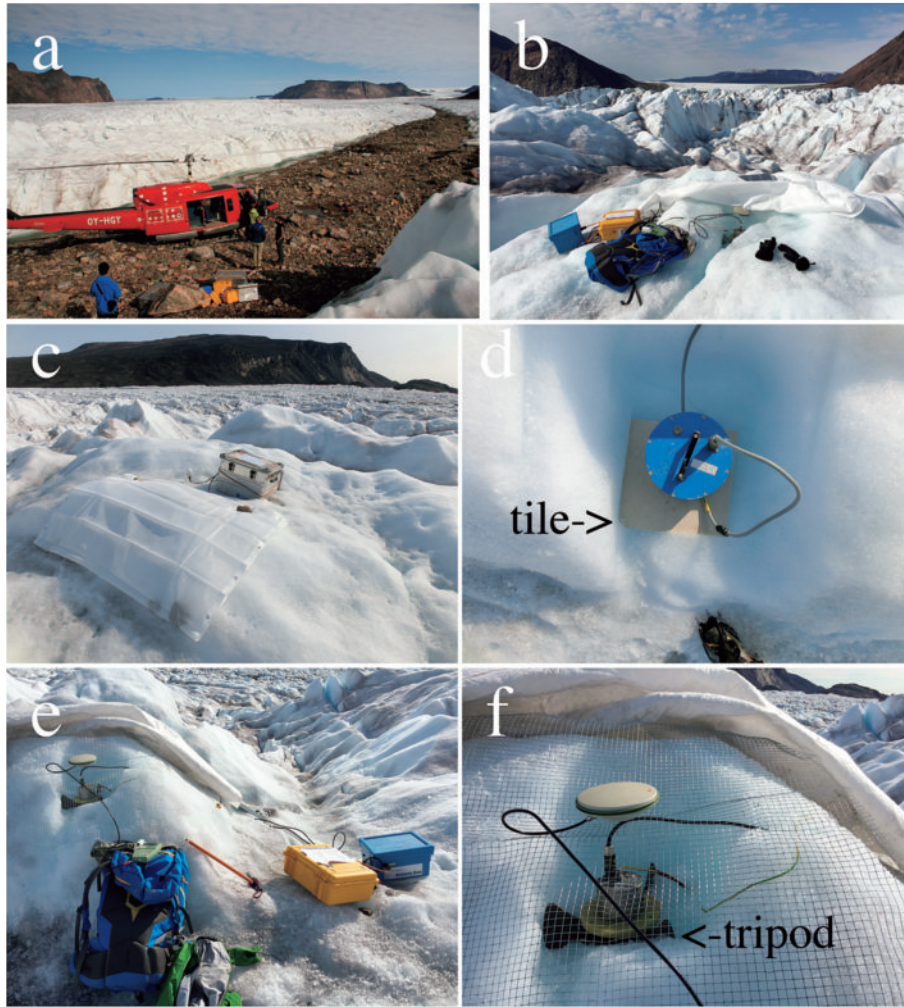


Figure 2 : (a) Staging area for seismic equipment on the central moraine, unloaded from the helicopter. (b) Seismic station IC1. An SP seismometer was screwed to a disk and placed on a metal tripod. Note the drainage channel for removing meltwater from the ice pit. The yellow watertight box contains the Taurus recorder, GPS antenna, and solar panel regulator. This box is connected to one external battery (Cyclon; 12V, 46 Ah) and a solar panel. (c) Seismic station ICC. An LP seismometer was placed in an ice pit and covered with a mesh and protective blanket. The aluminum Zarges box contains the Guralp recorder, battery (Fiamm, 12V, 42 Ah), and solar panel regulator. The solar panel and GPS antenna are located at the sides of the box. (d) LP seismometer at station ICC deployed on a ceramic tile. (e) Seismic station IC2; setup is as for station IC1 — see (b) above. (f) SP seismometer at station IC2, deployed on a metal tripod. Note that the Leica Geosystems dual-frequency GPS antenna is placed into an intentionally formed depression in the mesh so that a consistent measurement position can be obtained. This strategy was also employed at station IC1. Efforts were always made to ensure that other parts of the mesh were kept away from direct contact with the cable.

a longitudinal profile of ice speed along Bowdoin Glacier. Seismic station IC1 was co-located with one of these GPS stations. Finally, Vaisala WXT520 and Campbell CR1000 automatic weather stations (AWS) were used to record meteorological conditions near the base camp, east of the glacier. A second time-lapse camera operating at 6 frames per hour was deployed at the base camp to monitor erosion of a glacier margin due to the river from the Mirror Glacier. All instruments were powered with 12 V batteries that were constantly charged by solar panels.

Finally, we note that all four on-ice seismic stations

were visited on a daily basis to enable maintenance tasks such as leveling, orientation, and data back-up to be performed. This ongoing effort was required due to intense ablation of the glacier surface of up to 45 mm w.e. per day, which is approximately equivalent to 5 cm of ice per day. Because the receivers moved with the ice flow a total distance of ~ 18 m during the campaign (Fig. 1), the precise location of each seismometer was re-measured with a dual-frequency GPS receiver every couple of days (Fig. 2e and f). We also note that calm weather conditions with almost no wind prevailed during our survey, providing a low-noise environment for

observations. These calm weather conditions were especially favorable for the acquisition of infrasound records, which are strongly affected by wind.

3. Results and discussion

3.1 Instrument performance

Maintenance of on-ice seismometers deployed in a zone of ablation is known to be a challenging and laborious task (Pomeroy et al., 2013). During our campaign, for example, we walked an >8 km round trip every day between the base camp and the seismic array to maintain the array. This maintenance work is dramatically different to the annual station visit that is typically required in classical seismology. Nevertheless, it is valuable if on-ice installations can be sustained via such regular visits, as they can provide superior data to that obtained at nearby stations deployed on bedrock. This difference in data quality arises because seismic arrivals recorded by on-ice stations have not experienced changes due to propagation through the complex ice-sediment-rock interface, whose seismic velocity structure is poorly understood. Finally, considering the relatively short duration of the campaign, daily visits guaranteed the success of data collection by reducing the risk of data loss due to possible troubles with the instruments, as well as allowed to continuously re-evaluate the performance of our setup.

Some difference was noted between the performance of the tripod and ceramic tile seismometer-supports, which are shown for comparison in Figures 2d and 2f. A tile was used only for the LP seismometer (Fig. 2d), simply because the latter was larger and heavier than the more compact SP sensors. On the one hand, tripods have sharp legs (Fig. 2f) that favor heterogeneous pressure-melting of the ice, potentially resulting in rapid loss of proper instrument leveling and orientation. On the other hand, tripods provide relatively stable conditions that reduce the risk of the sensor falling. The tile, however, in our opinion better preserves the level of the instrument, because the load is distributed more evenly and thus pressure melt is fairly homogeneous under the tile area. Nevertheless, the flat and smooth bottom of the tile may allow the instrument to slowly drift to the side of a pit, which creates a risk of

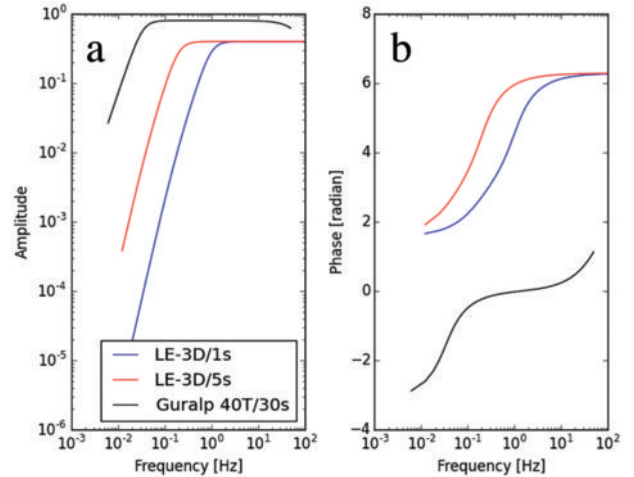


Figure 3 : Frequency response of the seismometers used in this study: (a) amplitude response; (b) phase response.

the sensor toppling if the pit has an open side. A further benefit of using tripods over tiles is that seismometers attached to disks and seated on tripods can be easily and quickly leveled and oriented. Seismometers deployed on tiles, however, require each of the three leveling screws to be adjusted individually. (It is worth mentioning that there is also the possibility to place the tripod on the tile, a practice adopted on Alpine glaciers).

We found that for all on-ice stations, degradations in instrument levels and rotations of up to ± 10 – 30° from north can sometimes occur within 24 hours, thereby reducing the fidelity of horizontal components for further analysis. For this reason, we discuss only the vertical-component traces recorded by the instruments (the vertical component is affected too, although less so).

The instrument response functions of the SP, LP, and broadband sensors used in this study differ from one another (Fig. 3), which means our dataset spans a wide frequency band with flat instrument response ranging from 0.033 to 100 Hz. Although most seismic signals were at frequencies above 0.5 Hz, the broadband instrument was valuable for documenting low-frequency events, as well as tele-seismic earthquakes that would otherwise have been missed. Moreover, the LP sensor installed on the glacier surface provided an opportunity to expand the frequency band of the seismic observations and, therefore, to obtain a more complete dataset.

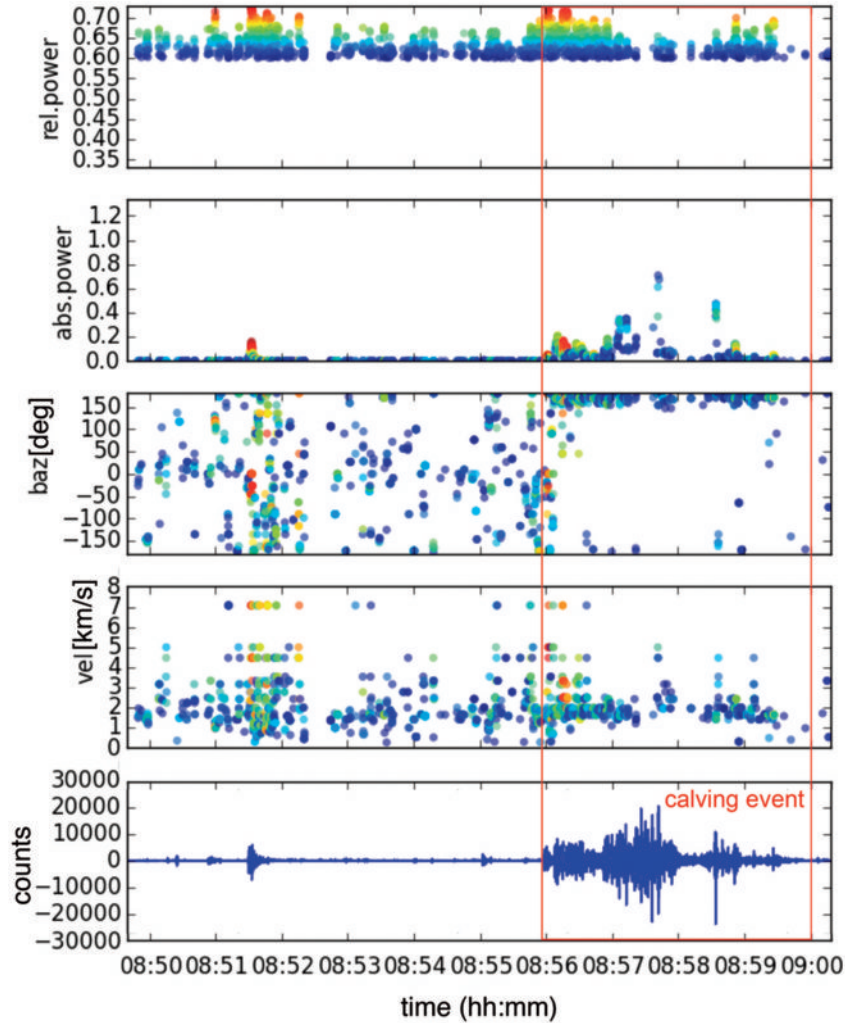


Figure 5 : Results of f - k analysis of a calving event for data in the interval 08 : 50 : 00–09 : 00 : 00 UTC on 18 July 2015 (using a sliding window of duration 1 s, a window fraction of 0.1 s, and frequency band of 1–10 Hz). Panels from top to bottom respectively show: relative power (i.e., equivalent of coherence); absolute power ($\times 10^{14}$; related to an amplitude of a signal) back-azimuth relative to north; apparent velocity (km/s); and the low-pass filtered (i.e., < 10 Hz) data trace. Marker colors in the upper four sub-panels correspond to the relative power from the top sub-plot (high relative power implies more reliable result).

synthetic sound. Multiple smaller-amplitude signals corresponding to ice-quakes are apparent in the video, in addition to the major event due to calving. Following the calving event, note the tsunami that is generated at the coast and the brownish melt-water plume that emanates from beneath the central part of the glacier. As shown by this video and Fig. 4c, the majority of seismic-energy release is due to long-period events and calving; however, the time-lapse video confirms that only calving can be observed visually and all other seismic activity is not accompanied by any recognizable processes at the calving front.

Array analysis, in particular frequency-wavenumber or f - k analysis, can be used to obtain the so-called back-azimuth; i.e., the angle of wave-front ap-

proach relative to north, together with slowness (i.e., the inverse of apparent velocity, $1/V_{\text{app}}$) at which the wave-front propagates through the array (Schweitzer et al., 2002; Rost and Thomas, 2002). Calving and other events recorded using our array can be analyzed using this method. A description of limits of the array resolution can be found in Appendix A.

An example of f - k analysis performed for four stations is shown in Fig. 5. The estimated back-azimuth (Fig. 6, energy in the direction 150–170° clockwise from north) points to the real location of the calving event of 18 July 2015, which is known from time-lapse photography. Further analysis of data for the full duration of the campaign will be published elsewhere.

Here, it is also worth mentioning that, according to

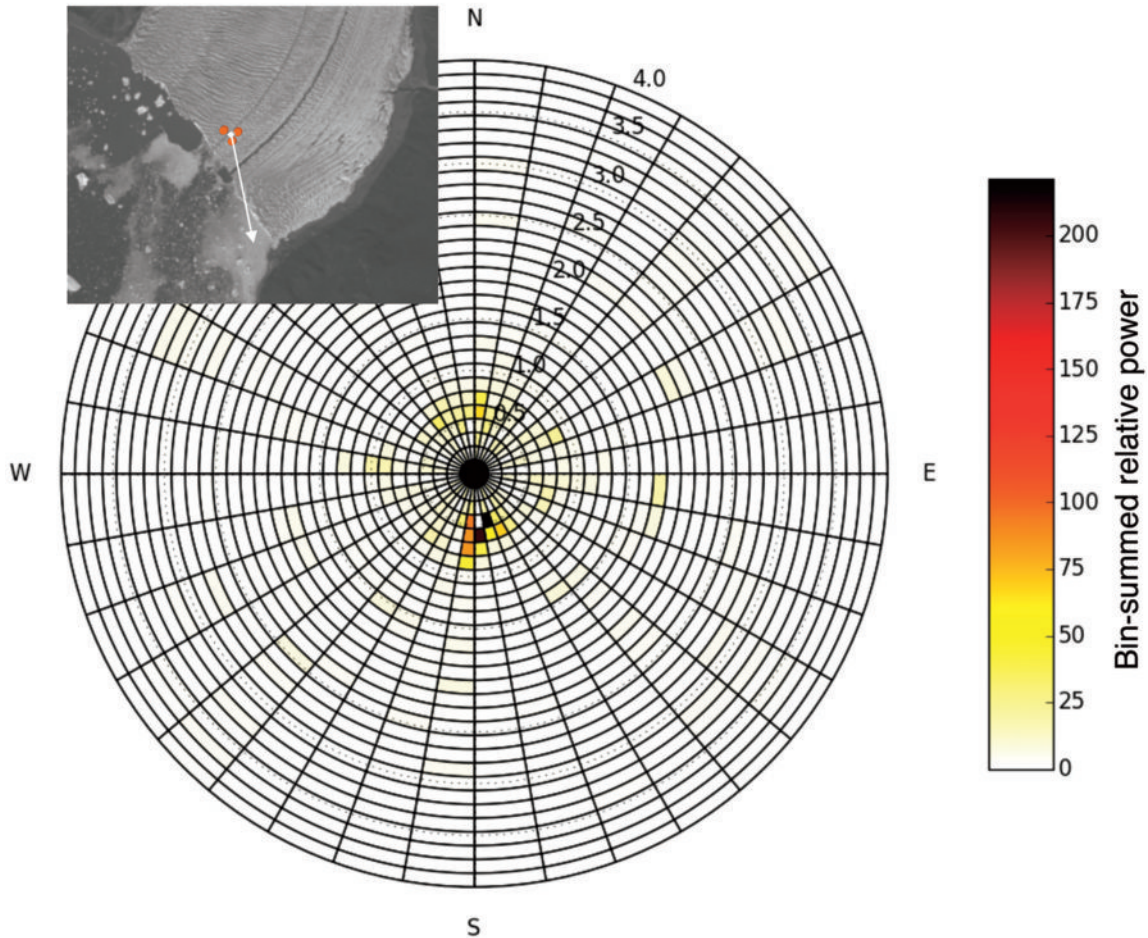


Figure 6 : Polar plot showing back-azimuth and slowness calculated using $f-k$ analysis of the calving event of 08 : 50 : 00–09 : 00 : 00 UTC on 18 July 2015, with cumulative relative power in gridded bins. The inset indicates the back-azimuth on the map.

our time-lapse records, some seismic tremor-like signals that are followed by micro-tsunamis (e.g., after 06 : 04 : 00 UTC on 17 July 2015) may not originate at the calving front, but from iceberg capsize in the fjord, which generates similar signals. The signals can be misinterpreted as calving, as was also reported by Richardson et al. (2010), who detected many false “calving events”.

3.2.1 Long-period events

Long-period (hereafter LP) events, with frequencies below 5 Hz, have puzzled seismologists and glaciologists since they were first detected, when it was realized that signals of glacial origin emanating from glacier-covered volcanoes can be confused with volcanic events (Weaver and Malone, 1976; St. Lawrence and Qamar, 1979). This type of event has regularly resurfaced in the literature over the last 40 years, and the debate surrounding the underlying mechanism is ongoing. Their source mechanism is usually explained as an analogy to volcanic

events, with brittle fracture-opening followed by resonance of a water-filled cavity or rapid flow of water into a newly opened space (Metaxian, 2003; West et al., 2010). Recently, LP events near Ekström and Roi Baudoin ice shelves, Antarctica, were found to occur exclusively on the rising tide and interpreted as basal fracturing due to upward bending of the ice shelf under tidal forcing (Hammer et al., 2015; Lombardi et al., 2016). The most recent Antarctic study by Lombardi et al. (2016) has encouraged further research into these LP events and their long-term variation. We observe a significant number of signals in our data set that resemble LP events (Fig. 7). The key features of LP events at Bowdoin Glacier are as follows:

- low-frequency content (i.e., < 10 Hz),
- long duration (up to 30 s and longer),
- monochromatic coda tail (around and below 1 Hz).

Furthermore, the amplitude of LP signals is larger than that of the majority of high-frequency events.

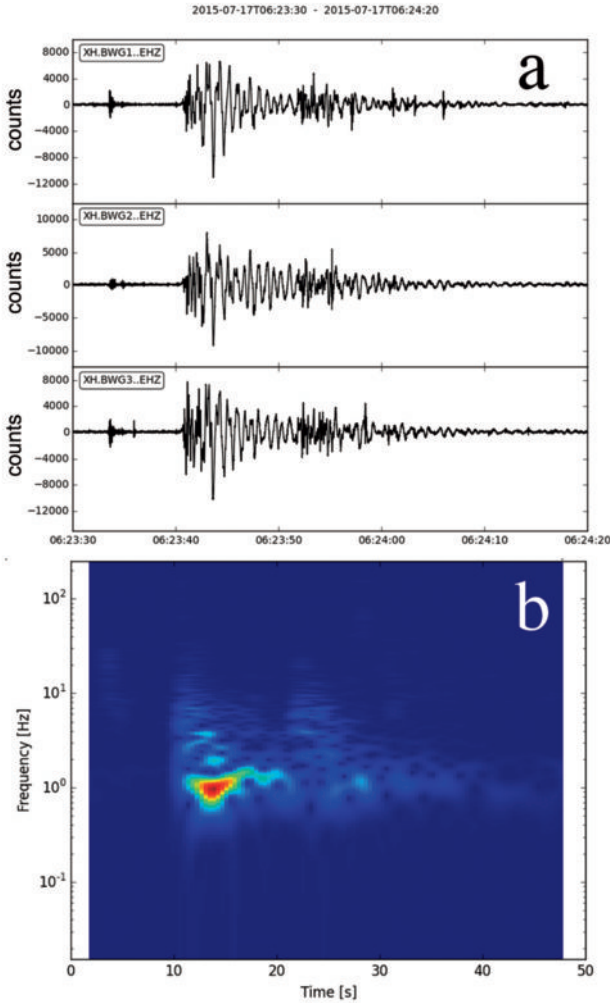


Figure 7 : (a) Example of a long-period event that occurred on 17 July 2015, which was recorded on the vertical component of three SP seismometers deployed on the glacier. (b) Spectrogram from station IC1 for the corresponding time interval.

Therefore, LP events can be seen at all seismic stations, including the broadband seismometer located on rock (Fig. 8). The true source mechanisms of LP events at Bowdoin Glacier remain to be understood, but should be obtainable through further analysis of long-term observations, as explained below.

3.2.2 Anomalous events

Amongst other noticeable events, two tele-seismic earthquakes were recorded, as well as several tremors with distinct gliding spectral lines (as illustrated below). These types of cryospheric phenomena are important for two reasons: (i) it is known that the passage of surface-wave arrivals from large tele-seismic earthquakes through the Antarctic ice sheet can trigger bursts of ice-quakes due to dynamic induced strains (Peng et al., 2014);

and (ii) it has been observed that ice sheet sliding and icebergs can produce long-duration tremors (e.g., with duration from 20 mins to 16 hours) with multiple harmonics. This latter phenomenon was previously interpreted as scratching of the ocean floor by icebergs (MacAyeal et al., 2008), or as the overlap of many small stick-slip events during large-scale slip of the Willans Ice Stream in Antarctica (Winberry et al., 2013; Lipovsky and Dunham, 2015). Similar tremors have also been reported in volcanic environments. Moreover, it is known that this type of event can be easily confused with helicopter tremors produced by rotor blade noise (Eibl et al., 2015), and we find this to be exactly the case in our records from Bowdoin Glacier, as shown in the analysis below.

3.2.2.1 Tele-seismic earthquakes

The vertical-component traces of two tele-seismic earthquakes recorded by broadband seismometer CFH on July 10 and 18 are shown in Fig. 9a and b. The parts of the signal with highest amplitude are associated with surface wave arrivals. These earthquakes can also be seen in records from the Thule permanent broadband station (station code: DK TULEG, GLISN), which is located ~ 125 km away (Fig. 9c and d). According to the European-Mediterranean Seismological Centre global event catalogue (www.emsc-csem.org), these earthquakes originated from an area to the east of Papua New Guinea (for details see Appendix B), at a distance of $\sim 12,000$ km from Bowdoin (i.e., an epicentral distance of $\sim 107^\circ$):

10 July 2015 04:12:41 UTC: M6.8 - Solomon Islands,

18 July 2015 02:27:33 UTC: M6.9 - Santa Cruz Islands.

The tele-seismic signals are dominated by low frequencies, meaning that the on-ice seismometers recorded only the ballistic, high-frequency-rich first-arrivals, as the rest of the signal bandwidth was below the instrument response (Fig. 10). At this preliminary stage of analysis we have not observed any evidence for increased ice-quake activity triggered by the tele-seismic surface-wave arrivals, which have previously been hypothesized as corresponding to the largest amplitude strains (Peng et al., 2014). Moreover, according to the time-lapse

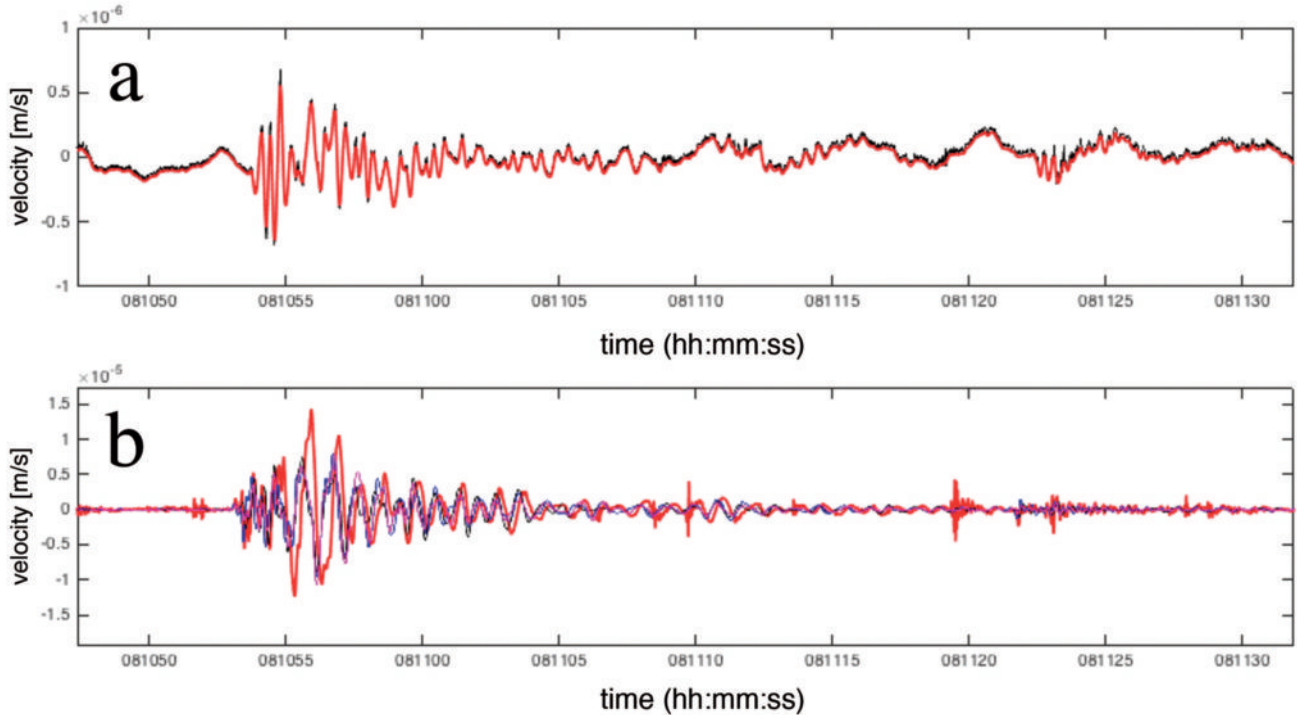


Figure 8 : (a) Long-period event that occurred on 18 July 2015, recorded at the broadband seismometer station CFH. Raw and low-pass-filtered (i.e., < 5 Hz) data are shown by black and red lines, respectively. (b) The same event as recorded by the on-ice stations, after application of the same lowpass filter. Data from the LP sensor are shown in red, with SP sensor data shown in other colors.

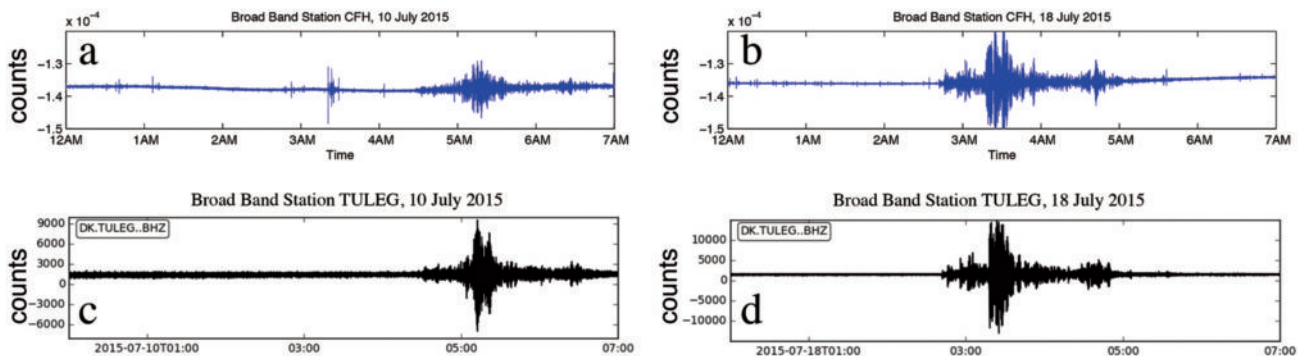


Figure 9 : (a, b) Raw traces recorded by temporary broadband station CFH for two tele-seismic earthquakes that occurred on 10 and 18 July 2015. This station was deployed on bedrock close to the calving front of Bowdoin Glacier. (c, d) Raw traces recorded on the same two days at the closest permanent broadband station TULEG (operated as part of Danish Seismological Network and GLISN), which is located ~ 120 km from the glacier (http://ds.iris.edu/SeismiQuery/by_station.html).

camera records, no calving events were observed during the passage of these long duration seismic trains through the site.

3.2.2.2 Harmonic tremor with spectral gliding

On 13 July 2015 a calving event was preceded by high-frequency harmonic tremor accompanied by spectral gliding (Fig. 11). This tremor event lasted for at least 175 s and was observed at all on-ice stations. The tremor and calving events overlapped in time for half of the calving-tremor duration (i.e., ~ 80 s). The tremor

shows a downward dip in the time-frequency plane, with between ~ 16 and 19 overtones being apparent beneath the Nyquist frequency of 250 Hz. In general, the overtones were regularly spaced as $f/f_0 = [\text{integer}]$; the interval between overtones was $\sim 12.2 \pm 0.7$ Hz.

Previous studies of helicopter-induced tremors (e.g., Eibl et al., 2015) reported that “helicopter-generated tremor consists of regularly repeating pulses”, has “fundamental frequencies above 10 Hz and overtones at integer multiples”, that the “Doppler Effect causes the frequency gliding”, and that “signals could be misinter-

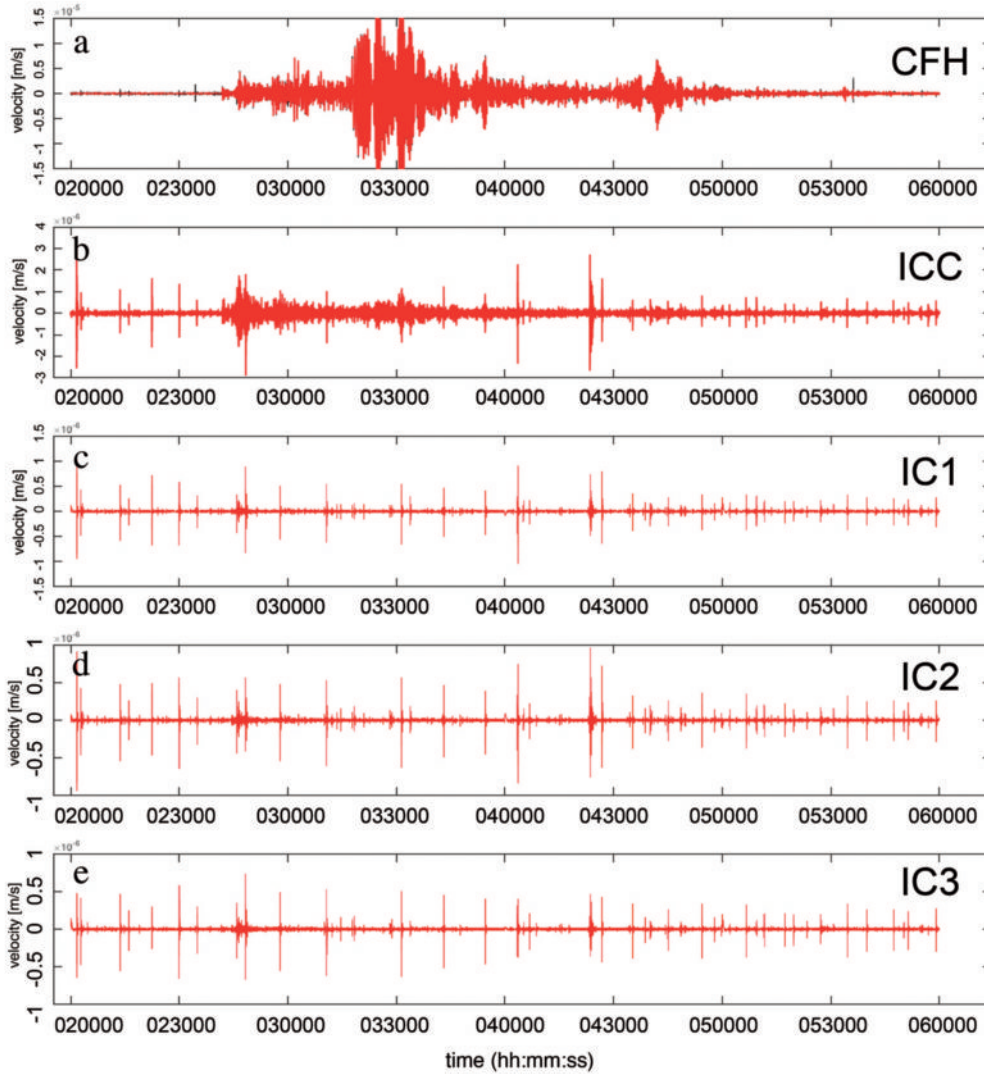


Figure 10 : Low-pass filtered seismogram (i.e., <0.5 Hz) showing the tele-seismic earthquake of 18 July 2015 as recorded by the Bowdoin seismic network at (a) broadband station CFH; (b) LP on-ice station ICC; and (c, d, e) SP on-ice seismometers IC1, IC2 and IC3, respectively. The step-like impulsive feature that is visible at 4:00 a.m., especially in sub-panels c and d, is a boundary effect due to filtering in hourly segments and is therefore an artifact.

interpreted as volcanic tremor on poorly monitored volcanoes.” In this light, all of the aforementioned features indicate that this tremor was artificially generated by a helicopter’s rotor.

Helicopter activity on 13 July 2015 can be reconstructed from a diary kept by the first author and the time-lapse camera, from which the following time line can be obtained. On this day, an Air Greenland Bell 212 helicopter, with an 1800 H.P. power unit and a rotor diameter of 14.63 m, arrived at the base camp at around 15:58 UTC. It would appear that this initial approach towards the base camp generated the tremor that overlapped the calving event. The helicopter arrived to pick up a Swiss TV crew to fly them over the glacier terminus to film two of our members standing near the

ice cliff. Later, between 16:32 and 16:45 UTC, the helicopter flew over the team members in a series of three loops. During the second fly-by, which occurred close to the seismic array, harmonic tremors were again observed (Fig. 12). It appears that before 16:00 UTC the calving front was partially covered with fog, which obscured this calving event from being recorded by the time-lapse camera. Members of the expedition who were staying at the central moraine near to the ice cliff (MF and SS) noted that they heard a loud calving noise. This noise emanated from a direction consistent with the back-azimuth derived from $f-k$ analysis, which was directed approximately towards the section of the calving front located between the western margin and the central moraine (Fig. 13).

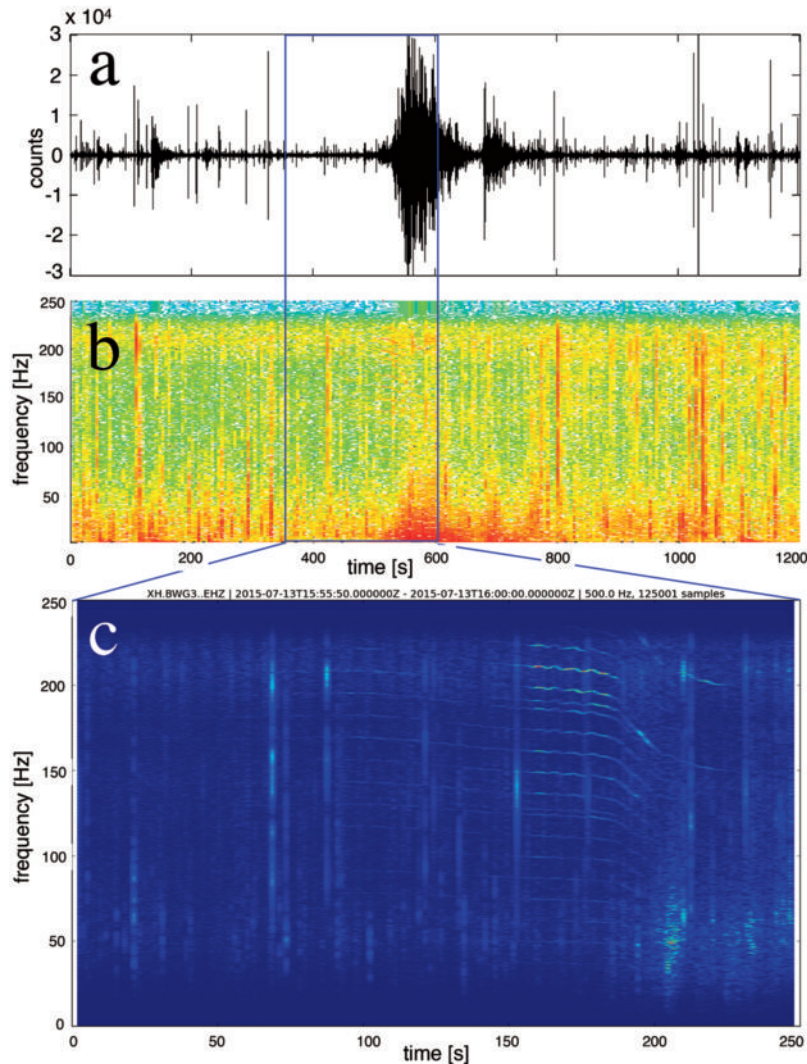


Figure 11 : Raw seismic trace (a) for the interval 15:50–16:10 UTC on 13 July 2015 from station IC1, and its spectrogram (b) showing the emergent signal of the calving tremor, which is preceded by a harmonic gliding tremor with overtones. (c) Close-up of the spectrogram of the same signal after it has been bandpass filtered between 50 and 250 Hz.

3.3 Temporal variations in seismic activity

Using the classic seismological technique of short-term averaging/long-term averaging (STA/LTA), we investigate and compare the temporal variations in seismic activity detected by the SP seismometers. Details of this analysis have recently been reported by Podolskiy et al. (2016). The most striking feature was the distinct tidal modulation of micro-seismic activity over a period of two weeks. The results show a double-peak diurnal oscillation in the number of events, with a maximum of up to 600 events per hour occurring during falling or low tides. Using high-resolution GPS measurements of surface displacement, we showed that the correlation between the number of events and tidal activity is transmitted through strain-rate variation (Fig. 14). The strain rate corresponds to local extension-

al stretching of the glacial surface, occurring mainly in response to increases in air temperature and falling tide velocity, which reduce back-pressure on the ice cliff. The increase in extensional strain rate is favorable for tensile co-seismic fracturing. A cartoon depicting this mechanism is shown in Fig. 15. Additional details are available in the original paper (Podolskiy et al., 2016).

3.4 Infrasound events

The infrasound array (Fig. 1) operated continuously from 8 to 19 July 2015, during which time several thousand infrasound coherent signals (hereafter called “events”) were recorded, emanating from various sources and directions. Analysis of these events reveals the existence of three main types of signal, with distinctive waveforms and source areas (Fig. 16). Here,

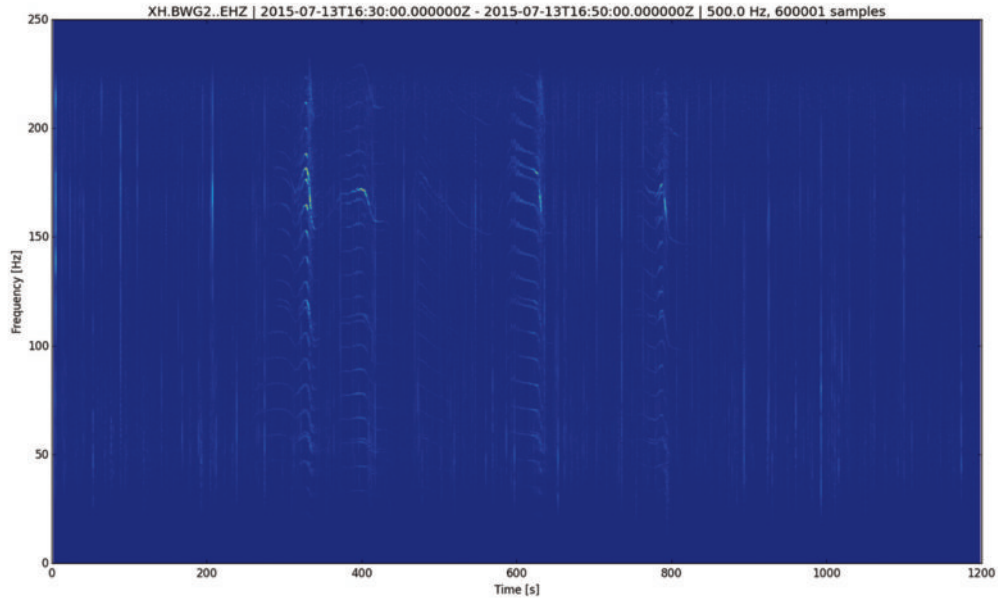


Figure 12 : Spectrogram of the harmonic gliding tremor signal generated by a helicopter (recorded at station IC2 for the period 16 : 30–16 : 50 UTC on 13 July 2015 after bandpass filtering between 50 and 250 Hz).

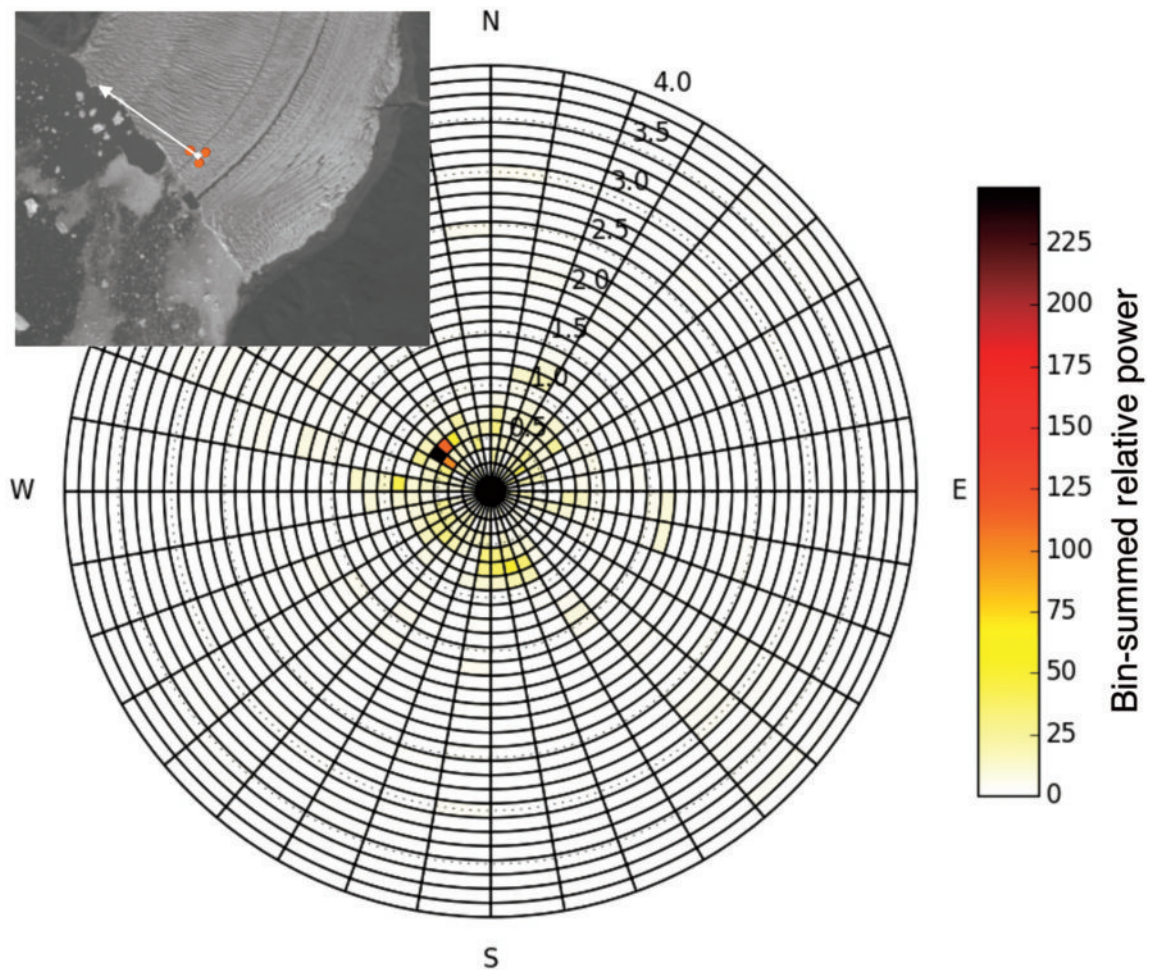


Figure 13 : Polar plot showing back-azimuth and slowness for the calving event of 15 : 50 : 00–16 : 00 : 00 UTC on 13 July 2015, determined from $f-k$ analysis with cumulative relative power plotted in gridded bins. The inset indicates the back-azimuth on the map.

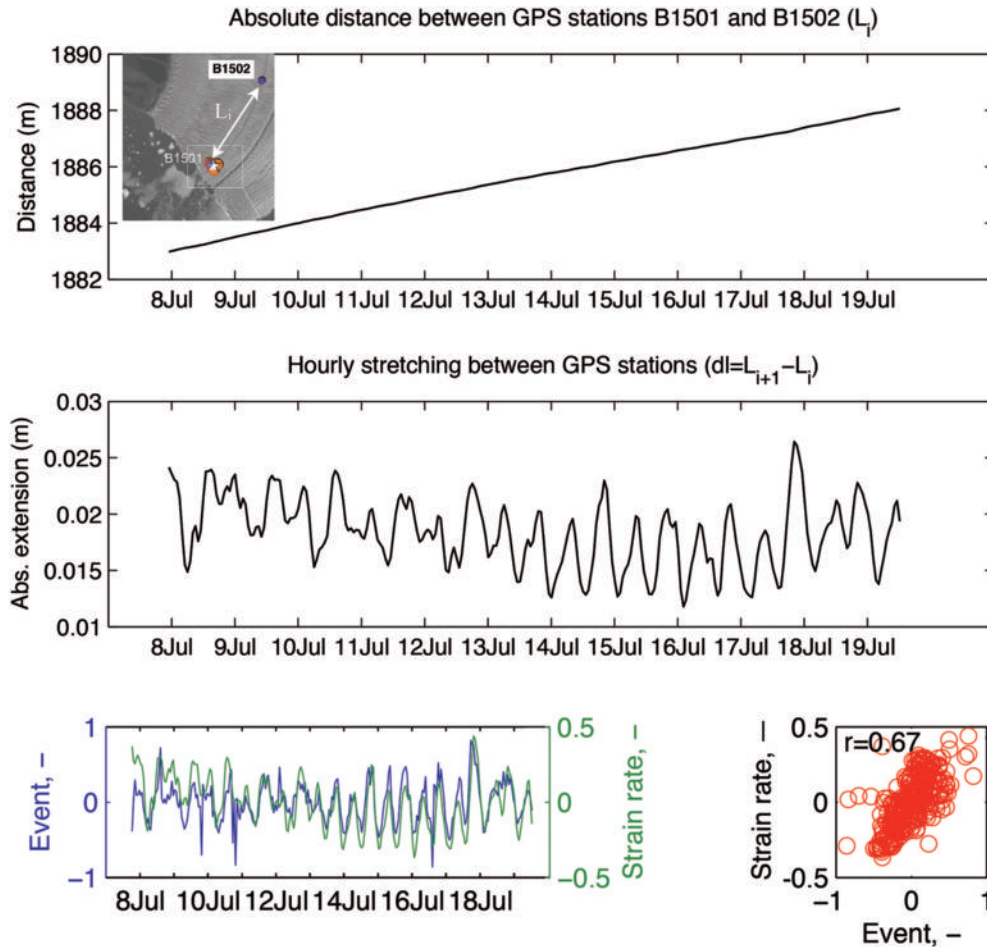


Figure 14 : Absolute and hourly extension of the glacier ice surface between GPS stations B1501 and B1502. The plot at lower left shows this extensional strain as an anomaly (i.e., a deviation from the mean) against the anomaly in a number of seismic events; the scatter plot at lower right shows that the correlation coefficient between the strain and the seismic activity is 0.67 (after Podolskiy et al., 2016).

several examples of the most typical (i.e., frequent) types of infrasound events and their characteristic waveforms are briefly introduced. More detailed analyses of the infrasound activity will be published elsewhere (Genco et al., in prep.).

3.4.1 Infrasound array analysis

The full infrasound dataset was processed using multichannel cross-correlation analysis. This method allows for the automatic discrimination of coherent signals from noise using a coherency threshold (e.g., Ripepe and Marchetti, 2002) and is based on the assumption that real infrasound signals will be coherently recorded at the different sensors of the array, while noise will not show any correlation across the array (Marchetti et al., 2015). This procedure was applied to the entire dataset using a sliding window of length 3 s and a 0.3 s shift between successive windows. The

data in each window are characterized in terms of the back-azimuth and apparent velocity of the energy contained within the window as well as a coherency index, which can be used to discriminate between windows containing signal and noise (Ulivieri et al., 2011). Examples of the results produced using this technique are shown in Figure 17.

The array processing technique was repeated using infrasound data filtered in different frequency bands, which revealed that the coherent signal is concentrated in the 0.5–10 Hz frequency range and shows a peak in the 1–5 Hz band, as is consistent with other observations on mass-movement-related phenomena, such as snow/ice avalanches (e.g., Bedard, 1989; Ulivieri et al., 2011) or calving events (Richardson et al., 2010). A total of $\sim 13,000$ detections (i.e., individual three-second windows with a coherency index exceeding the threshold) were extracted from the ~ 260 hours of continuous

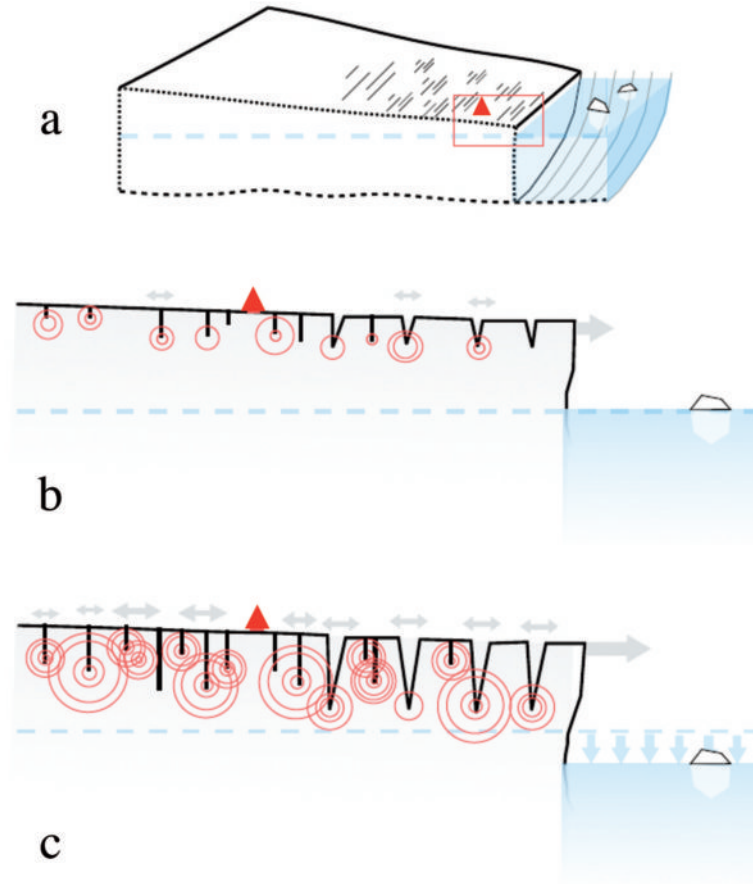


Figure 15 : Cartoon showing the dominant mechanism driving micro-seismic activity at Bowdoin Glacier: (a) longitudinal cross-section of the glacier with an on-ice seismometer shown by the red triangle; (b) the crevassed area near the calving front at high tide; (c) the same area near the calving front at low tide.

infrasound recording. Over 90% of the detections fall into three distinct back-azimuth sectors, suggesting three main source areas (Fig. 16a). Differences in waveforms, durations, and amplitudes of signals originating from these different sectors suggest the existence of different source processes for each of the observed signal types, as also confirmed by seismic data, time-lapse photography, and direct observations (Fig. 16b-c). In the following subsections, these three sources are introduced and discussed. We note that the aforementioned helicopter traverse (section 3.2.2) over some stations of our infrasound network (e.g., ICC at 16:34–16:44 UTC on 13 July 2015) also produced distinct artificial signals with clear monochromatic spectral content.

3.4.2 Calving-front events

Before introducing calving-front events, we need to remind that infrasound and seismic waves are sensitive to different source physics (Richardson et al., 2010). In

general, infrasound is generated by mass acceleration leading to displacement of air volume, while seismic signals are mainly produced by release of elastic energy through brittle failure of material or slip, and, in case of calving, an interaction of icebergs with water, ice and the ocean floor (for a detailed discussion of calving seismic emissions see Podolskiy and Walter, 2016).

The largest azimuthal sector from which infrasound signals are observed, spanning back-azimuths of 220° – 266° (Fig. 16c), coincides with the full extent of the Bowdoin Glacier calving front, which is situated between 2950 and 3700 m from the center of the infrasound array (Fig. 1). Despite the limited number of signals recorded in this sector (i.e., 2.2% of the total number of detections), this class of event is interesting in terms of the complexity of the recorded waveforms, duration of the events, and the amount of energy released. Analysis of the infrasound-array data identified 33 calving-front events with durations spanning from a few seconds to several minutes. Sixteen of these events are clustered

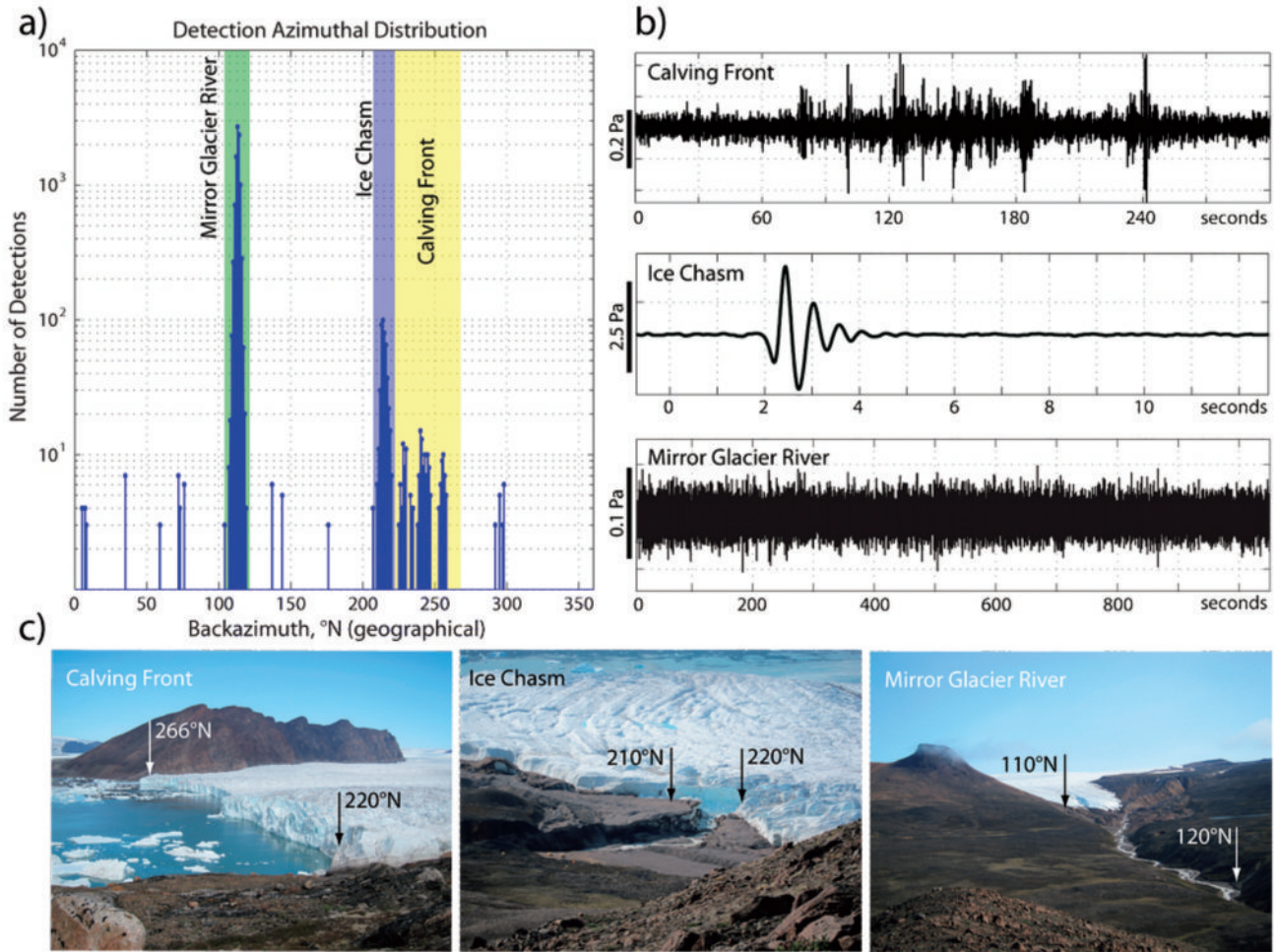


Figure 16 : (a) Number of detected infrasound events as a function of back-azimuth, with different source sectors highlighted by colored bars. (b) Example of infrasound signals produced by calving-front (top), ice-chasm (middle) and Mirror Glacier River (bottom) events. (c) Photographs of the identified source areas, annotated with back-azimuth ranges with respect to the array center, for the calving-front (left), ice-chasm (center) and Mirror Glacier River (right) events.

in three main calving episodes: July 10, 03:21–03:26 UTC; July 13, 15:58–16:03 UTC; July 18, 08:56–09:00 UTC. The other 17 events are shorter in duration and often consist of a single pulse or only a few pulses. All of the recorded events show amplitudes below 1 Pa at the HLL array, but are also clearly recorded at stations ICC and CFH with comparable amplitudes. Assuming a sound velocity of 320–330 m/s, which is reasonable for air temperatures between 0 and 10°C, the time delay between the three sites (Fig. 18) and source back-azimuth with respect to the array are compatible with a source located on the calving front. This analysis therefore provides strong evidence that calving is the process generating these events. Seismic records, time-lapse camera images and direct field observations confirmed that these infrasound signals were generated by calving events. For example, Figure 17 shows the

infrasound signature of the seismic event presented in Figure 5 (i.e., July 18, 2015) for the same time window. The infrasound-array analysis provides a back-azimuth of 225–230°N, which is comparable with the source position obtained from f - k analysis of seismic-array data that was also validated using time-lapse photography (see section 3.2). Closer inspection of the infrasound traces reveals that each calving event, and particularly those with longer durations, consists of multiple discrete pulses of short duration that repeat at intervals of a few seconds, and sometimes merge into a continuous oscillatory phase with a duration of a few seconds. Spectral analysis shows that the main frequency content of these signals is between 0.5 and 5 Hz, peaking at ~ 2 Hz, which is consistent with seismic observations.

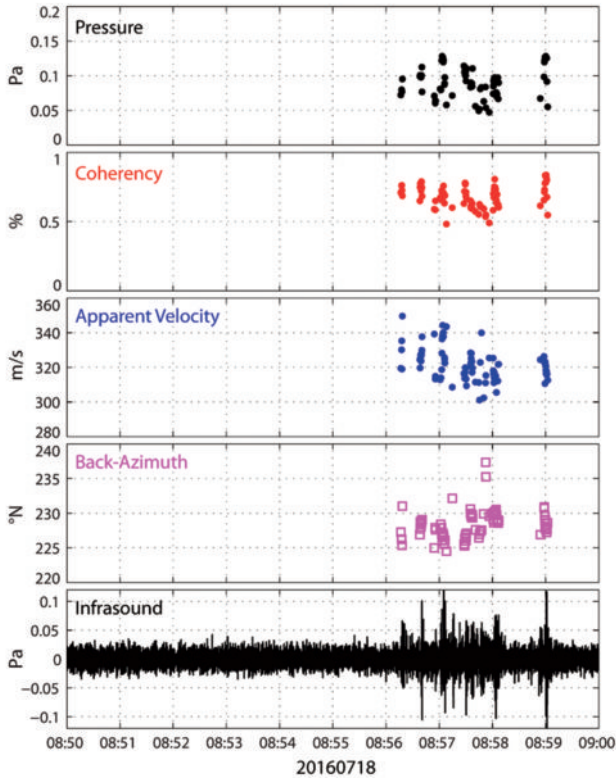


Figure 17 : Results of the multichannel cross-correlation analysis performed on infrasound data in the 1–10 Hz frequency band using a sliding window of length 3 s and a 0.3 s shift between successive windows. Acoustic pressure, coherency, apparent velocity, back-azimuth and infrasound trace data (band-pass filtered in the 1–10 Hz band) are plotted for the same time period as shown in Figure 5 (i.e., 08 : 50 : 00–09 : 00 : 00 UTC, 18 July 2015).

3.4.3 Ice-chasm events

Close to base camp, at the location where the proglacial stream emanating from the terminus of Mirror Glacier enters Bowdoin Glacier to become a subglacial stream, an ice chasm and a gorge have formed that are prone to collapse (Fig. 16c). The morphology of this ice chasm area evolved during the observation period via repeated serac falls, which produced clearly audible sounds, as well as sharp infrasound pulses that were recorded by the nearby HLL array. The more energetic ice-falls were also recorded at the more distant stations ICC and CFH. These ice-chasm events are characterized by simple waveforms that consist mainly of a single pulse, sometimes followed by a short coda of a few oscillations, with a maximum total duration of a few seconds (Fig. 16b). Peak amplitudes are generally higher than those seen for calving-related events, but are significantly reduced at stations ICC and CFH, where signals from ice-chasm events are often barely observ-

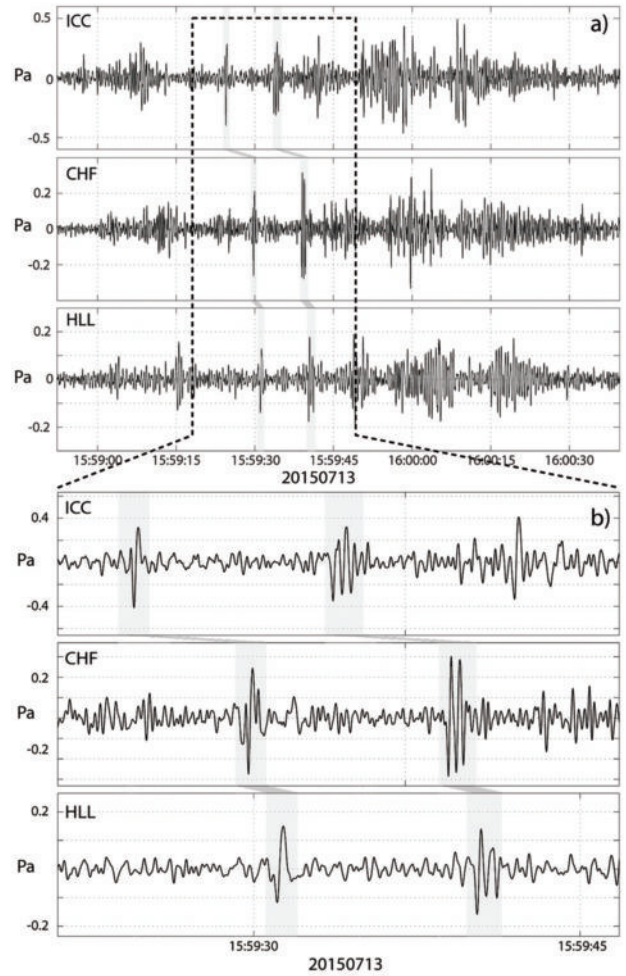


Figure 18 : (a) Infrasound signals (i.e., pressure) for the calving event of July 13, 2015 recorded at the ICC and CFH single-sensor stations and the HLL array. (b) Close-up view of the infrasound data for the highlighted time interval. Despite small differences in the character of the signal, the traces recorded at each of the three locations clearly show correlated pulses with constant time lags caused by the different source-receiver distances.

able. Infrasound signals from these events have a spectral content that shows a strong peak at frequencies between 2 and 3 Hz. The relationship between recorded infrasound signals and this ice-chasm source process was confirmed by direct observations, which were easily made due to the proximity of the ice-chasm to the base camp.

3.4.4 Mirror Glacier River events

Surprisingly, the vast majority of detected events (i.e., 87%) are associated with signals that have very small amplitudes and back-azimuths between 110 and 120°N. These azimuths are consistent with the position of a turbulent river that flows from the terminus of

Mirror Glacier (Fig. 16c). These signals are barely detectable, lack a characteristic waveform signature, have amplitudes that are comparable to the noise level, and are not continuously detected over the observation period. Rather, these signals are detected from time to time in episodes lasting a few hours, whereby the events increase in number and amplitude before eventually subsiding (detailed analysis will be published elsewhere). These events have a relatively broad frequency content in the 1–20 Hz band. The absence of a well-defined waveform signature and the emergent nature of these signals seem to suggest that these events are related to changes in stream flow, and may in fact reflect changes in the melting rate of Mirror Glacier. However, this hypothesis needs further investigation.

4. Summary and outlook

This paper presents examples of seismic and infrasound records obtained during a short but fruitful geophysical experiment in July 2015 at Bowdoin Glacier in northwest Greenland. This data set has already provided important and novel insights into glacier dynamics (Podolskiy et al., 2016). Further analysis of the unique combination of seismic, infrasound, tsunami, and geodetic time series is ongoing, and will be published elsewhere (Genco et al., in prep.; Minowa et al., in prep.; Podolskiy et al., in prep.).

Seismic signatures (or lack thereof) from a variety of processes remain to be analyzed, including subglacial water tremor, since the array was located close to a turbulent meltwater plume, and a large-scale rifting event, which presumably started on 14 July 2015 and led to the major calving event of 27 July that occurred after the field campaign was concluded (Fig. 19). The plume and the rift activity may be related through subglacial melting, which could induce an additional downward bending moment on the overhanging ice cliff.

In July 2016 a more ambitious geophysical experiment was performed at Bowdoin Glacier, with a larger number of seismic and infrasound stations, deployed near or at the glacier to obtain short- and long-term observations. Eight infrasound sensors were arranged in pairs, forming an approximately triangular array at an elevation of 460 m at Sentinel Nunatak in front of the

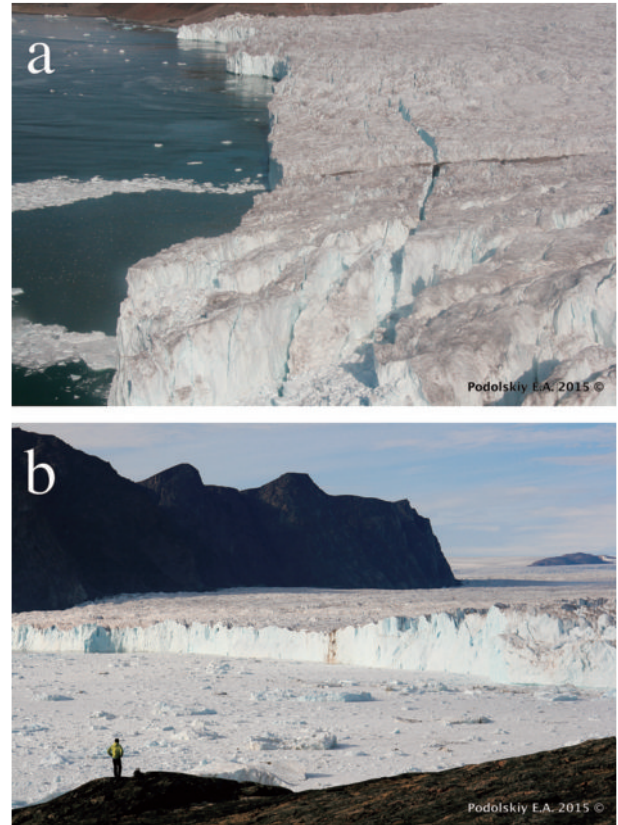


Figure 19 : Photographs of the calving front before and after the major calving event. (a) Meltwater plume and newly formed rift as seen from a helicopter on 20 July 2015; the white spots over the plume are feeding birds. (b) Calving front of Bowdoin Glacier after the calving event (28 July 2015).

glacier. Three time-lapse cameras and a radar were also installed. At the same time, eight seismic stations were deployed directly onto the ice in two triangular arrays. One array, consisting of four short-period Lennartz LE-3D/1s seismometers, was located approximately at the same location as in 2015 (Podolskiy et al., 2016); the other was set ~ 1.5 km up-flow of the first. This second ‘upper’ seismic array included one Lennartz LE-3Dlite MkIII/1s placed at the glacier surface and three Lennartz LE-3D/BHs borehole seismometers deployed at a depth of slightly less than 3 m. This depth was chosen to assure melt out in the next summer season. The seismometers were connected to DATA-CUBE³ recorders produced by Omnirecs (a GFZ spin-off company in Potsdam, Germany), two large Cyclon or Block-Power 65 Ah batteries, and solar panels. The borehole seismic array had an aperture of ~ 250 m and will be left in situ during winter 2016/17, with the recording system switched to energy- and memory-saving modes (i.e., cycled GPS recording at 50 samples

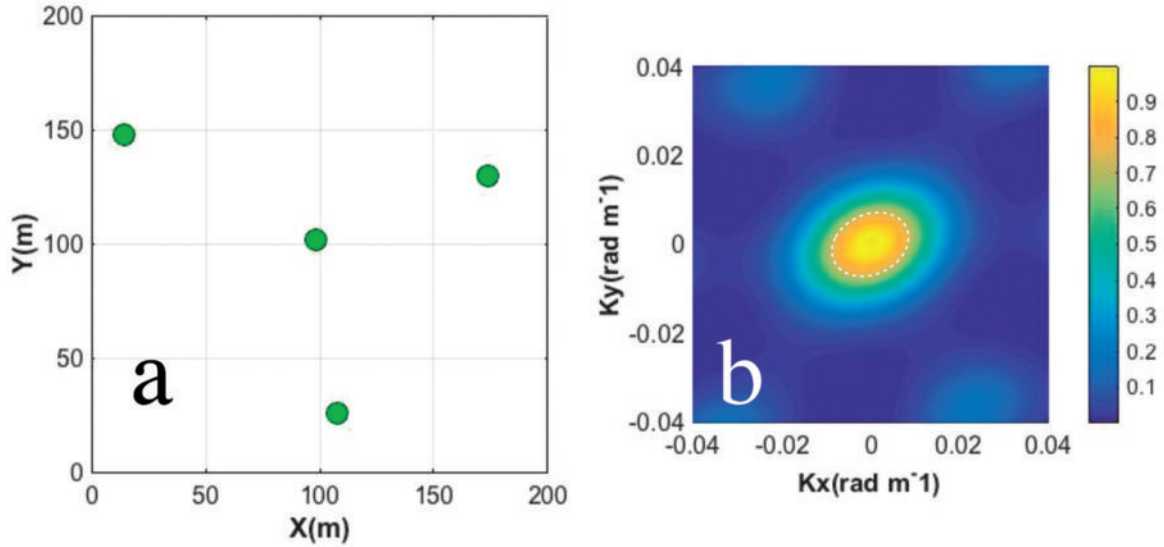


Figure A1 : (a) Geometry and (b) array response function of the Bowdoin Glacier on-ice seismic array computed at 1 Hz. Dashed ellipse indicates the resolution bounds.

per second for 4 out of every 40 minutes). Contrary to surface seismometers, the borehole sensors do not need maintenance. If the array performs well under the harsh polar-winter conditions, and instruments can be safely retrieved in July 2017, we anticipate gaining further valuable insights into long-term seasonal variations in glacier seismicity, especially related to changes in subglacial hydraulics and LP events. The experiment will also serve as an assessment of the performance of the compact, lightweight, and low-cost DATA-CUBE³ recorders in the challenging polar environment.

Appendix A: Bowdoin array response function

For understanding examples of array analysis and its limitations, we need to introduce the array response function (ARF) of our array (Fig. A1). This function represents the resolution quality of the array for signals of different frequency and slowness (e.g., Schweitzer et al., 2002; Rost and Thomas, 2002). For the geometry of our array (Fig. A1a), the largest observable (i.e., Nyquist) wavenumber k is, in theory, less than 0.04 rad m^{-1} , which corresponds to a shortest observable wavelength of 25 m (i.e., any shorter wavelengths will alias). The shape of the main ARF lobe (Fig. A1b) indicates that the relative power of the array response shows a rapid drop in the center, meaning that energy falling into the yellow region ($<0.006 \text{ rad m}^{-1}$) is suppressed. The longest

observable wavelength is approximately equivalent to the aperture of the array, or to $\sim 160 \text{ m}$, which means that at larger wavelengths the response of our array is equivalent to the response of any one station (i.e., all sensors are excited at the same time).

Appendix B: Tele-seismic earthquakes

The association of aforementioned tele-seismic earthquakes with particular recorded events at Bowdoin Glacier can be verified by estimating the arrival time of the fastest P wave arrivals, which were diffracted along the core-mantle boundary (i.e., the P_{diff} phase). For example, the first arrival at Thule for the signal seen on 10 July 2015 was at around 04:26:53 UTC (Fig. 10a), which is consistent with the ~ 14 minute travel-time that is predicted by the IASP91 Earth model (Fig. B1). Similarly, the first arrival at Thule on 18 July 2015 is seen at 02:41:53 UTC (Fig. 10b), which also corresponds to the expected 14 minute delay.

Acknowledgments

Some of the contents of this paper were presented by EAP and RG at the international workshop “Greenland Ice Sheet Mass Loss and its Impact on Global Climate Change”, held at the Institute of Low Temperature Science, Hokkaido University (Sapporo, Japan; 22–24 March 2016). The authors acknowledge

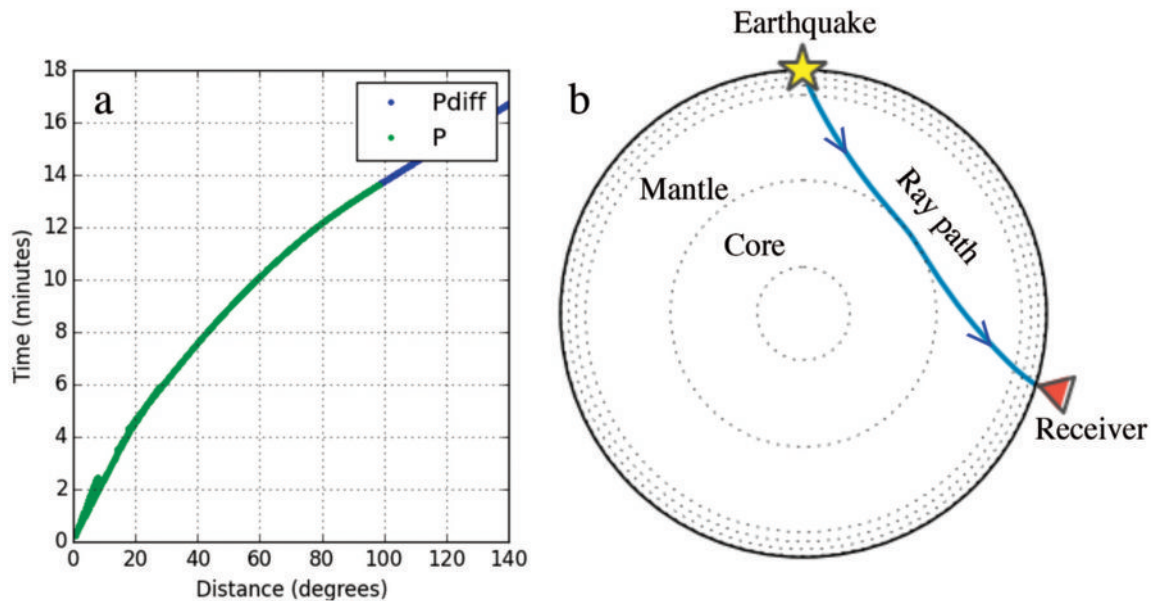


Figure B1 : (a) Travel-time curve predicting arrival time of the first seismic phase from an earthquake at a particular epicentral distance calculated using the IASP91 velocity model. In our case, source-receiver distance between epicenters in Oceania and seismic stations in the Qaanaaq region was around 107° , and the first arrival corresponded to the P_{diff} seismic phase. (b) The P and P_{diff} ray paths traced through the IASP91 velocity model.

funding from a JSPS fellowship (Grant-in-Aid PU15901), SNF grant 200021_153179/1, and the GREEN and ArCS projects. We also thank G. Lombardi for field support and the helicopter pilots of Air Greenland for their skills and logistical assistance in carrying out complex operations over the glacier surface. Signal processing and preparation of figures presented in this manuscript were performed using ObsPy, QGIS, and MATLAB software.

References

- Baldwin, E. B. (1896) *The Search for the North Pole or Life in the Great White World*. Chicago, Illinois, USA.
- Bartholomaus, T. C., J. M. Amundson, J. I. Walter, S. O'Neil, M. E. West, and C. F. Larsen (2015) Subglacial discharge at tidewater glaciers revealed by seismic tremor. *Geophys. Res. Lett.*, **42** (15), 6391–6398, doi: 10.1002/2015GL064590.
- Bedard, A. (1989) Detection of avalanches using atmospheric infrasound. In: *Proceedings of the Western Snow Conference*, B. Shafer (ed.), Western Snow Conference, April 1989, Colorado State University, Fort Collins, CO, USA, 52–58.
- Carmichael, J. D., I. Joughin, M. D. Behn, S. Das, M. A. King, L. Stevens, and D. Lizarralde (2015) Seismicity on the western Greenland Ice Sheet: Surface fracture in the vicinity of active moulins. *J. Geophys. Res. Earth Surf.*, **120** (6), 1082–1106, doi: 10.1002/2014JF003398.
- Chamberlin, T. C. (1895) Appendix A: Geology. In: H. G. Bryant, *The Peary Auxiliary Expedition of 1894* (reprint from *Bulletin of Geographical Club*, No.5), pp.29–56.
- Chamberlin, T. C. (1897) Glacial studies in Greenland. *X. J. Geol.*, **5** (3), 229–240.
- Eibl, E. P. S., I. Lokmer, C. J. Bean, E. Akerlie, and K. S. Vogfjörd (2015) Helicopter vs. volcanic tremor: Characteristic features of seismic harmonic tremor on volcanoes. *J. Volcanol. Geotherm. Res.*, **304**, 108–117, doi: 10.1016/j.jvolgeores.2015.08.002.
- Ekström, G., M. Nettles, and G. A. Abers (2003) Glacial earthquakes. *Science*, **302** (5645), 622–624, doi: 10.1126/science.1088057.
- Ekström, G., M. Nettles, and V. C. Tsai (2006) Seasonality and increasing frequency of Greenland glacial earthquakes. *Science*, **311** (5768), 1756–1758, doi: 10.1126/science.1122112.
- Hammer, C., M. Ohrnberger, and V. Schlindwein (2015) Pattern of cryospheric seismic events observed at Ekstrom Ice Shelf, Antarctica. *Geophys. Res. Lett.*, **42** (10), 3936–3943, doi: 10.1002/2015GL064029.
- IPCC (2013) *Climate Change 2013: The Physical Science Basis. Contribution of Working Group I to the Fifth Assessment Report of the Intergovernmental Panel on Climate Change* (eds. T. F. Stocker, D. Qin, G.-K. Plattner, M. Tignor, S. K. Allen, J. Boschung, A. Nauels, Y. Xia, V. Bex and P. M. Midgley). Cambridge University Press, Cambridge, United Kingdom and New York, NY, USA, 1535 pp.
- Khan, S. A., A. Aschwanden, A. A. Bjork, J. Wahr, K. K. Kjeldsen, and K. H. Kjaer (2015) Greenland ice sheet mass balance: a review. *Rep. Prog. Phys.*, **78** (4), 046801, doi:

- 10.1088/0034-4885/78/4/046801.
- Kogelnig, A., E. Suriñach, I. Vilajosana, J. Hübl, B. Sovilla, M. Hiller, and F. Dufour (2011) On the complementariness of infrasound and seismic sensors for monitoring snow avalanches. *Nat. Hazards Earth Syst. Sci.*, **11**, 2355–2370, doi: 10.5194/nhess-11-2355-2011.
- Lipovsky, B. P., and E. M. Dunham (2015) Tremor during ice stream stick-slip. *Cryosphere Discuss.*, **9** (5), 5253–5289, doi: 10.5194/tcd-9-5253-2015.
- MacAyeal, D. R., E. A. Okal, R. C. Aster, and J. N. Bassis (2008) Seismic and hydroacoustic tremor generated by colliding icebergs. *J. Geophys. Res.*, **113** (F3), F03011, doi: 10.1029/2008JF001005.
- Marchetti, E., M. Ripepe, G. Olivieri, and A. Kiogelnig (2015) Infrasound array criteria for automatic detection and front velocity estimation of snow avalanches: towards a realtime early warning system. *Nat. Hazards Earth Syst. Sci.*, **15**, 2545–2555, doi: 10.5194/chess-15-2545-2015.
- Metaxian, J. -P. (2003) Seismicity related to the glacier of Cotopaxi Volcano, Ecuador. *Geophys. Res. Lett.*, **30** (9), 1483, doi: 10.1029/2002GL016773.
- Mordret, A., T. D. Mikesell, C. Harig, B. P. Lipovsky, and G. A. Prieto (2016) Monitoring southwest Greenland's ice sheet melt with ambient seismic noise. *Sci. Adv.*, **2** (5), doi: 10.1126/sciadv.1501538.
- Murayama, T., M. Kanao, M. Yamamoto, Y. Ishihara, T. Matsushima, and Y. Kakinami (2015) Infrasound array observations in the Lützow-Holm Bay region, East Antarctica. *Polar Sci.*, **9** (1), 35–50, doi: 10.1016/j.polar.2014.07.005.
- Lombardi, D., L. Benoit, T. Camelbeeck, O. Martin, C. Meynard, and C. Thom (2016) Bimodal pattern of seismicity detected at the ocean margin of an Antarctic ice shelf. *Geophys. J. Int.*, **206** (2), 1375–1381, doi: 10.1093/gji/ggw214.
- Peng, Z. G., J. I. Walter, R. C. Aster, A. Nyblade, D. A. Wiens, and S. Anandkrishnan (2014) Antarctic icequakes triggered by the 2010 Maule earthquake in Chile. *Nat. Geosci.*, **7** (9), 677–681, doi: 10.1038/ngeo2212.
- Preiswerk, L. E., F. Walter, S. Anandkrishnan, G. Barfucci, J. Beutel, P. G. Burkett, P. Dalban Canassy, M. Funk, P. Limpach, E. Marchetti, L. Meier, and F. Neyer (2016) Monitoring unstable parts in the ice-covered Weissmies northwest face. *INTERPRAEVENT 2016 – Conference Proceedings*, pp.434–443.
- Podolskiy E. A. and F. Walter (2016) Cryoseismology. *Rev. Geophys.*, **54** (4), 708–758, doi: 10.1002/2016RG000526.
- Podolskiy, E. A., S. Sugiyama, M. Funk, F. Walter, R. Genco, S. Tsutaki, M. Minowa, and M. Ripepe (2016) Tide-modulated ice flow variations drive seismicity near the calving front of Bowdoin Glacier, Greenland. *Geophys. Res. Lett.*, **43**, 2036–2044, doi: 10.1002/2016GL067743.
- Pomeroy, J., A. Brisbourne, J. Evans, and D. Graham (2013) The search for seismic signatures of movement at the glacier bed in a polythermal valley glacier. *Ann. Glaciol.*, **54** (64), 149–156, doi: 10.3189/2013AoG64A203.
- Richardson, J. P., G. P. Waite, K. A. FitzGerald, and W. D. Pennington (2010) Characteristics of seismic and acoustic signals produced by calving, Bering Glacier, Alaska. *Geophys. Res. Lett.*, **37** (3), L03503, doi: 10.1029/2009GL041113.
- Ripepe, M., and E. Marchetti (2002) Array tracking of infrasonic sources at Stromboli volcano. *Geophys. Res. Lett.*, **29**, 2076, doi: 10.1029/2002GL015452.
- Roeoesli, C., A. Helmstetter, F. Walter, and E. Kissling (2016) Meltwater influences on deep stick-slip icequakes near the base of the Greenland Ice Sheet. *J. Geophys. Res. Earth Surf.*, **121** (2), 223–240, doi: 10.1002/2015JF003601.
- Rost, S., and C. Thomas (2002) Array seismology: Methods and applications. *Rev. Geophys.*, **40** (3), 1008, doi: 10.1029/2000RG000100.
- Schweitzer, J., J. Fyen, S. Mykkeltveit, S. J. Gibbons, M. Pirli, D. Kühn, and T. Kvaerna (2012) Chapter 9: Seismic Arrays. In: Bormann, P. (ed.), *New Manual of Seismological Observatory Practice (NMSOP-2)*, IASPEI, GFZ German Research Centre for Geosciences, Potsdam, doi: 10.2312/GFZ.NMSOP-2_CH9.
- Sugiyama, S., D. Sakakibara, S. Tsutaki, M. Maruyama, and T. Sawagaki (2015) Glacier dynamics near the calving front of Bowdoin Glacier, northwestern Greenland. *J. Glaciol.*, **61** (226), 223–232, doi: 10.3189/2015JoG14J127.
- St. Lawrence, W., and A. Qamar (1979) Hydraulic transients: a seismic source in volcanoes and glaciers. *Science*, **203** (4381), 654–656.
- Olivieri, G., E. Marchetti, M. Ripepe, I. Chiambretti, G. De Rosa, and V. Segor (2011) Monitoring snow avalanches in Northwestern Italian Alps using an infrasound array. *Cold Reg. Sci. Technol.*, **69**, 177–183, doi: 10.1016/j.coldregions.2011.09.006.
- Veitch, S. A., and M. Nettles (2012) Spatial and temporal variations in Greenland glacial-earthquake activity, 1993–2010. *J. Geophys. Res.*, **117** (F4), F04007, doi: 10.1029/2012JF002412.
- Walter, F., J. Chaput, and M. P. Lüthi (2014) Thick sediments beneath Greenland's ablation zone and their potential role in future ice sheet dynamics. *Geology*, **42** (6), 487–490, doi: 10.1130/G35492.1.
- Weaver, C. S., and S. D. Malone (1976) Mt. Saint Helens seismic events: volcanic earthquakes or glacial noises? *Geophys. Res. Lett.*, **3** (3), 197–200.
- West, M. E., C. F. Larsen, M. Truffer, S. O'Neel, and L. LeBlanc (2010) Glacier microseismicity. *Geology*, **38** (4), 319–322, doi: 10.1130/G30606.1.
- Winberry, J. P., S. Anandkrishnan, D. A. Wiens, and R. B. Alley (2013) Nucleation and seismic tremor associated with the glacial earthquakes of Whillans Ice Stream, Antarctica. *Geophys. Res. Lett.*, **40** (2), 312–315, doi: 10.1002/grl.50130.